nanomaterials

MDPI

Article

Facile Strategy for Synthesizing Non-Stoichiometric Monoclinic Structured Tungsten Trioxide (WO_{3-x}) with Plasma Resonance Absorption and Enhanced Photocatalytic Activity

Shihao Chen [1], Yang Xiao [1], Wei Xie [3], Yinhai Wang [1,*], Zhengfa Hu [2], Wei Zhang [1] and Hui Zhao [1]

1 School of physics & optoelectronic engineering, Guangdong University of Technology, Guangdong 510006, China; shchenbhx@163.com (S.C.); xiaoyxy1023@163.com (Y.X.); weizh55@gdut.edu.cn (W.Z.); kkhui@gdut.edu.cn (H.Z.)

2 Synergy Innovation Institute for Modern Industries, Guangdong University of Technology, Dongyuan 517500, China; zhfhu@gdut.edu.cn

3 School of Physics Science and Technology, Lingnan Normal University, Zhanjiang 524048, China; xiewei@lingnan.edu.cn

* Correspondence: yhwang@gdut.edu.cn; Tel.: +86-020-39322265

Received: 6 June 2018; Accepted: 17 July 2018; Published: 21 July 2018

Abstract: Oxygen vacancy defects play an important role in improving the light-capturing and photocatalytic activity of tungsten trioxide (WO_3). However, the hydrogen treatment method that is commonly used to introduce oxygen vacancies is expensive and dangerous. Therefore, the introduction and control of oxygen vacancy defects in WO_3 remains a challenge. Here, we demonstrated that oxygen vacancies could be successfully introduced into WO_{3-x} while using a facile method through low temperature annealing in alcohol. The obtained WO_{3-x} samples with optimal oxygen vacancies showed strong absorption of light, extending from the ultraviolet to the visible and near-infrared regions, and exhibits strong plasmon resonance from 400–1200 nm peaking at approximately 800 nm. When compared to pristine WO_3, the photocatalytic activity of WO_{3-x} was greatly improved in the ultraviolet and visible regions. This study provides a simple and efficient method to generate oxygen vacancies in WO_3 for photocatalysis, which may be applied in the photoelectrochemical, electrochromic, and photochromic fields. Because oxygen vacancy is a common characteristic of metal oxides, the findings that are presented herein may be extended to other metal oxides.

Keywords: oxygen vacancies; WO_{3-x} nanosheets; photocatalysis; plasmon resonance absorption; photodegradation

1. Introduction

Semiconductor photocatalysis has attracted significant attention due to its promising applications in solar energy conversion, since the discovery of water splitting on a titanium dioxide (TiO_2) photoanode in the 1970s [1]. However, the photocatalytic efficiency of TiO_2 is limited by its large band gap energy and fast electron-hole recombination due to its high density of trap states [2,3]. Great efforts have been dedicated to enhancing the visible light absorption of large band gap metal oxides. For instance, dye-sensitized and noble metal nanodot decorated TiO_2 nanostructures were developed [4,5], forming heterojunctions with other semiconductors [6,7], and band gap narrowing was achieved via elemental doping in order to improve the conversion efficiency of metal oxide photoelectrodes. These methods modified the optical absorption coefficient and wavelength of the

materials [8–10]. In addition to studies on reducing the band gap of TiO_2 for enhanced visible light response, alternative semiconductor materials (WO_3, ZnO, SnO_2, $ZnGaO_4$, and $BiVO_4$) with intrinsic narrow band gaps are currently being explored [11–14]. Among them, tungsten trioxide is an attractive semiconductor material.

Tungsten trioxide (WO_3) exhibits powerful oxidation properties, non-toxicity, and low cost and it has found widespread applications in electrochromic devices [15], gas sensors [16,17], photoelectrochemical water splitting, and photodegradation of organic compounds [18–22]. However, the photocatalytic activity of pristine WO_3 is not high enough for practical use. Therefore, different strategies have been developed to increase the photocatalytic activity of WO_3, including the preparation of WO_3 with different nanostructures [23], supporting noble metal Pt/Au/Ag [24–26], composites with other materials [27–29], and oxygen vacancy defects [30–34]. The introduction of oxygen vacancies is a simple and efficient strategy to improve the photocatalytic performance of WO_3 and it can greatly increase its conductivity and the absorption of visible light by local surface plasmon resonance (LSPR) in the near-infrared region, yielding an intensity that is comparable to bandgap absorption [35,36]. Over the past decades, persistent efforts have focused on improving the photocatalytic activity of WO_3 by introducing oxygen vacancies, and various strategies have been proposed. At present, the main method for introducing oxygen vacancies is through the hydrogenation of WO_3 [31,37]. Chen et al. produced black TiO_2 using hydrogen treatment of white TiO_2 in 2011, which triggered a surge in the production of hydrogenated semiconductors [38] and vacuum annealing procedures [37]. For instance, Yamashita et al. reported a facile H-spillover route to prepare heavily hydrogen-doped WO_3 (H_xWO_3) [39]. These hydrogenated H_xWO_3 materials exhibited strong plasmonic absorption in the visible light region, which is tunable over a wide range by varying its stoichiometry. The electron concentration of the hydrogenated sample was high, up to 3.1×10^{21} cm^{-3}. Gong et al. explored the exfoliation of layered tungstic acid to form WO_3 nanosheets, and prepared sub-stoichiometric WO_3 single crystal nanosheets, and subsequently introduced oxygen vacancies [35]. Simultaneously, the introduction of oxygen vacancies can promote the separation of photo-generated electrons and holes and inhibit their recombination, thus improving photocatalytic activity [40]. Therefore, the introduction of oxygen vacancies in WO_3 plays an important role in photocatalytic performance. However, these methods require harsh experimental conditions and are expensive, which make them difficult to perform in most laboratories. Consequently, WO_3-based semiconductors with adequate activity under visible or solar light are still under investigation.

Herein, we prepared monoclinic structured WO_3 nanosheets via a one-step template-free hydrothermal route and then introduced oxygen vacancies through low temperature annealing in alcohol. These processes successfully synthesized non-stoichiometric monoclinic structured WO_3 (WO_{3-x}) nanosheets. Because of the introduction of oxygen vacancies, the WO_{3-x} showed enhanced electron concentrations of up to 9.1×10^{21} cm^{-3}, which are enough to induce LSPR. The WO_{3-x} also exhibited very strong visible and infrared light absorption, which significantly increased its photocatalytic activity.

2. Experimental

2.1. Preparation of the WO_3 Nanosheets

The WO_3 single crystal nanosheets were synthesized by a one-step template-free hydrothermal route [41]. Sodium tungstate dehydrate ($Na_2WO_4 \cdot 2H_2O$, 0.6398 g, 2 mmol) was added into distilled water (40 mL) and hydrochloric acid (40% HCl, 20 mL, adjusted pH = 1.5) was subsequently added into the Na_2WO_4 solution at room temperature (25 °C), stirring with vigorous magnetic for approximately 10 min. Then, the mixture was transferred to a 100 mL Teflon-lined stainless-steel autoclave. The autoclave was sealed and incubated at 180 °C for 12 h and then subsequently cooled down to room temperature naturally. The final products were collected by centrifuging the mixture, washed several times with distilled water and absolute ethanol, and drying at 60 °C in air.

2.2. Preparation of WO_{3-x} Nanosheets

In a simple synthetic procedure, the prepared green-yellow WO_3 nanosheets (0.5 g) were added into 10 mL absolute ethanol to form a suspension. After vigorous stirring for 10 min, the suspension was poured into a sintering boat (length 6 cm, width 3 cm, height 1.5 cm) and transferred to a vacuum tube furnace (SK-G06163, Φ60/50 × 1000 mm). The ends of the vacuum tube are sealed. The initial temperature is set to 50 °C, and the temperature is raised at a rate of 5 °C/min until the temperature reaches 400 °C, and the temperature is maintained at 400 °C for three hours. Then, the temperature is lowered at a rate of 5 °C/min until the temperature reaches 50 °C, and hence, cooled down to room temperature naturally. The obtained grey powders were collected for further characterization.

2.3. Characterization

The X-ray diffraction (XRD) patterns were recorded by X-ray diffractometer (D8 ADVANCE, BRUKER) with Cu-K_α radiation (λ = 1.541 Å) in a wide angle range from 10° to 80° on 2θ scale. Field emission scanning electron microscopy (FE-SEM) images, which were collected on a Hitachi SU8220 electron microscope with a working distance of 8 mm. Transmission electron microscopy (TEM) images and high-resolution TEM images were performed by using a FEI TecnaiG2 F20 with an acceleration voltage of 200 kV and TEM sample specimens were prepared by briefly ultrasonicating the sample powders in ethanol, followed by placing a drop of the suspension onto lacey support films that were dried before imaging. Fourier transformed infra-red (FT-IR) measurements were carried out using a 80/80 v Bruker TENSOR27 spectrometer. The FT-IR spectra were acquired with KBr discs under transmission mode. The scanned wavenumber range was from 4000 to 400 cm^{-1}. The Raman spectra were recorded on a RENISHAW A-9570-2000 Raman spectrometer with an excitation wavelength of 785 nm. UV-Vis diffuse reflectance spectroscopy (DRS) measurement was conducted by a SHIMADZU UV-3600 spectrophotometer. X-ray photoelectron spectra (XPS) were recorded on a THERMO ESCALAB 250 Xi with a monochromatic Al K_α X-ray source. The electron paramagnetic resonance spectra were recorded while using a JES-FA200 spectrometer at room temperature.

2.4. Photocatalytic Test

2.4.1. UV Light Photocatalytic Degradation

Rhodamine B (RhB) is an organic dye with a bright red colour and it is widely used as a model pollutant in photocatalytic tests. Therefore, the photocatalytic activity of the WO_{3-x} nanosheets samples was evaluated in terms of the decolorization of RhB dye under UV irradiation from a 500 W Hg lamp. The lamp was positioned in a cylindrical Pyrex vessel and cooled by circulating water to maintain the reaction temperature at approximately 27 °C. A quartz tube was used as the photo catalytic reactor. The catalysts (0.02 g) were dispersed into 40 mL of 2×10^{-5} M RhB solution and stirred in the dark for 20 min to reach a complete adsorption–desorption equilibrium between the photocatalyst and RhB solution. Then, the mixture was exposed to UV light. Vigorous magnetic stirring was maintained to keep WO_{3-x} nanosheets suspended in the RhB solution. The concentration of aqueous RhB was determined with a UV-Vis spectrophotometer by measuring the absorption peak intensity at 553 nm.

2.4.2. Visible Light Photocatalytic Degradation

The photocatalytic activity of WO_{3-x} nanosheets under visible light was also evaluated by monitoring the decomposition of RhB. The apparatus for studying the photocatalytic decomposition of RhB was identical under visible and ultraviolet light, except that an 800 W Xe lamp with a 420 nm cut-on filter was used instead of a Hg lamp as the light source.

3. Results and Discussion

3.1. Characterization of the WO_{3-x} Nanosheets

The WO_{3-x} single crystal nanosheets were prepared by a one-step template-free hydrothermal route and oxygen vacancies were introduced through low-temperature annealing in ethanol. It is well-known that ethanol has reducing properties. When annealing WO_3 in ethanol (anaerobic environment), ethanol can consume oxygen atoms in WO_3, resulting in oxygen vacancies in the crystals. This strategy is simple, safe, and efficient when compared to the hydrogen treatment of WO_3. The fabrication procedure of stable WO_{3-x} nanosheets is schematically illustrated in Figure 1a. Meanwhile, the annealing process was accompanied by a strong colour change from the original light yellow WO_3 to the final grey WO_{3-x} (Figure 1b). This method can be used in most laboratories and mass production of WO_{3-x} can also be achieved. The obtained WO_{3-x} exhibits very good stability, as no change was observed after storage for six months. We performed detailed characterizations and photocatalytic performance tests of the prepared catalyst, as follows.

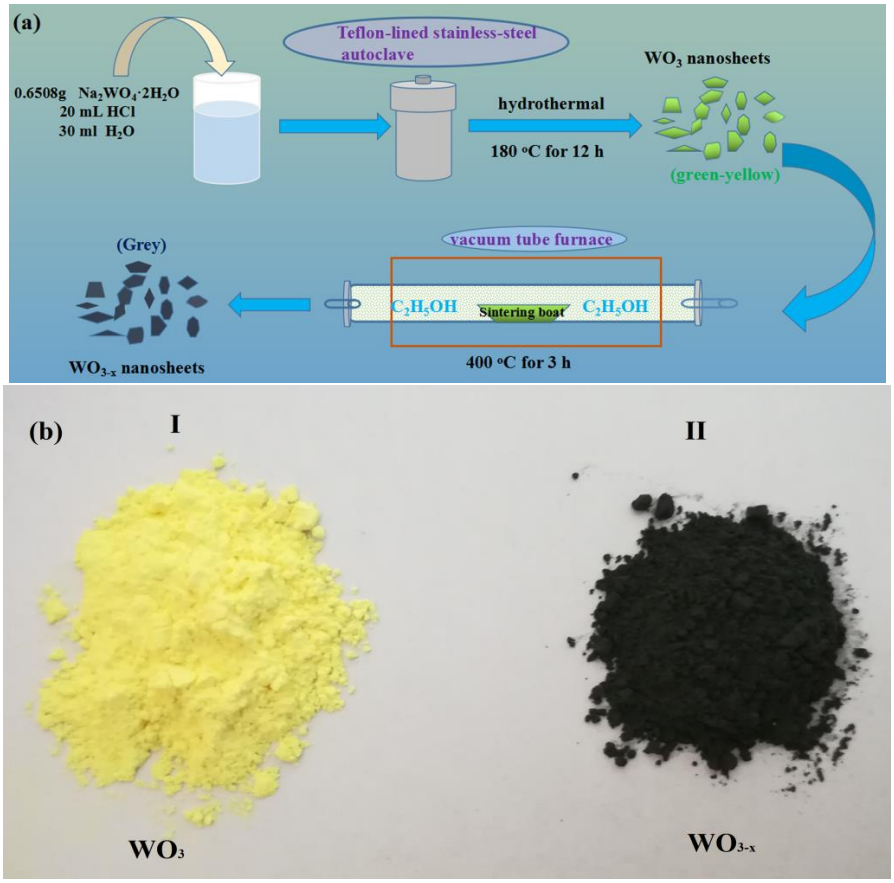

Figure 1. (**a**) Schematic illustration of the fabrication of tungsten trioxide (WO_3) and non-stoichiometric monoclinic structured WO_3 (WO_{3-x}) nanosheets. (**b**) Digital photos of the WO_3 (I) and WO_{3-x} (II) nanosheets samples.

The morphologies of the WO_3 and WO_{3-x} samples were examined by FE-SEM and field emission transmission electron microscopy (FE-TEM), as shown in Figure 2. The SEM and TEM images clearly show the stacking morphology of the WO_3 nanosheets and no obvious change in the size and morphology was observed after annealing. The thickness of the nanosheets was typically 20–30 nm, with a length of 100–150 nm. In addition, the similar morphologies of WO_3 (Figure 2a,c) and WO_{3-x} (Figure 2b,d) prove that the annealing treatment at 400 °C does not significantly change the nanosheet

morphology of WO_{3-x}. As shown in the representative HR-TEM image of an unannealed WO_3 nanosheets (Figure 2e), clear lattice fringes can be identified, and the lattice fringe spacing between two adjacent crystal planes is 0.38 nm, corresponding to the (002) lattice plane of the monoclinic structured WO_3 [42]. In contrast, the framework of the highly crystalline WO_{3-x} can be clearly observed in Figure 2f, and the WO_{3-x} nanosheets also crystallize well and have a lattice spacing of 0.38 nm between the (002) planes.

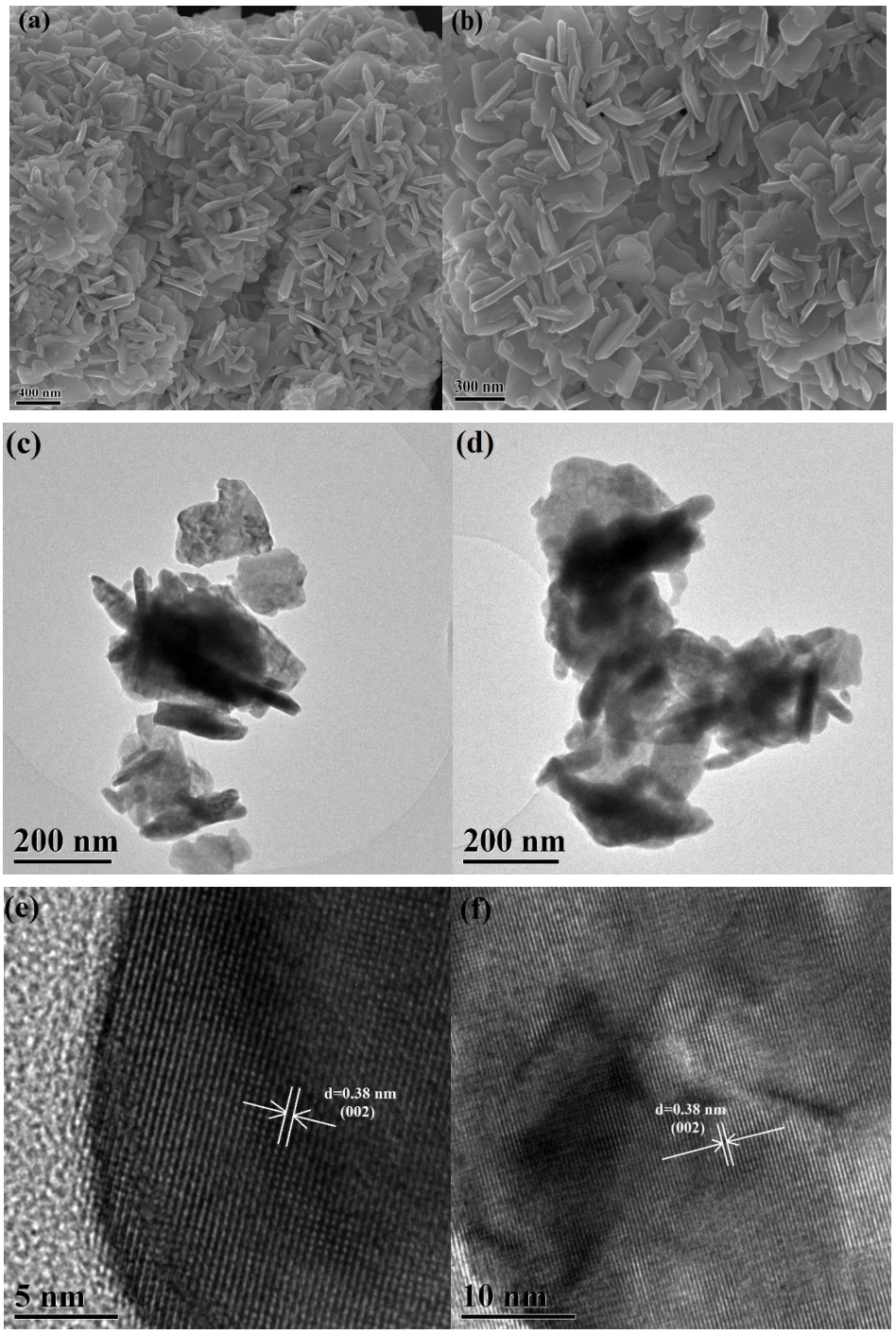

Figure 2. Field emission scanning electron microscopy (FE-SEM) images of the WO_3 (**a**) and WO_{3-x} (**b**) nanosheets. FE-TEM images of the WO_3 (**c**) and WO_{3-x} (**d**) nanosheets. Field emission transmission electron microscopy (HR-TEM) images of the WO_3 (**e**) and WO_{3-x} (**f**) nanosheets.

The monoclinic crystal structure of the as-prepared WO_{3-x} and WO_3 samples were confirmed by the X-ray diffraction patterns shown in Figure 3a. The WO_3 and WO_{3-x} samples exhibited similar diffraction peaks, with peak centers at 23.1, 23.6, 24.3, 26.6, 28.7, 33.4, 34.1, 41.6, 50.1, and 55.9 corresponding to the (002), (020), (200), (120), (112), (202), (122), (222), (140), and (420) crystal faces of the monoclinic structured WO_3 that was indexed to the JCPDS card No. 43-1035 [43]. No characteristic peaks of other crystalline impurities were detected. In addition, no other crystalline forms of WO_3 were observed after low temperature annealing.

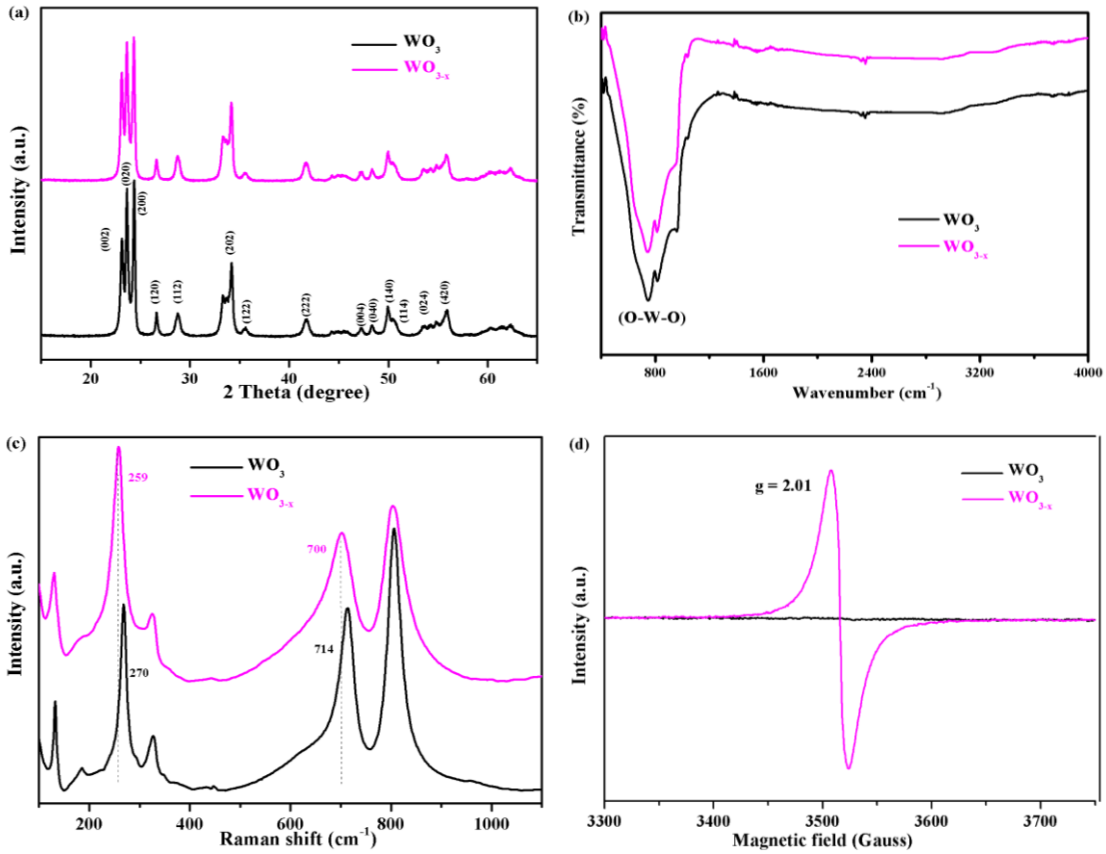

Figure 3. Comparison of the WO_3 and WO_{3-x} nanosheets. (**a**) X-ray diffraction (XRD) patterns; (**b**) Fourier-transform infrared spectroscopy (FTIR) spectra; (**c**) Raman spectra and (**d**) electron paramagnetic resonance (EPR) spectra at room temperature.

To further study the chemical structure and surface composition of the as-fabricated WO_{3-x} nanosheets, the samples were characterized, as shown in Figure 3b. Both samples only show a strong absorption peak at 800 cm^{-1}, which can be attributed to (O–W–O) of the interconnected octahedron WO_3 [44]. Meanwhile, no other characteristic peaks were observed after low temperature annealing. This indicates that no other chemicals or organic residues were present on the surface of the WO_{3-x} nanosheets after the fabrication procedure. Raman spectroscopy was performed to investigate the chemical structure of the samples, as shown in Figure 3c. The oxygen deficiencies of WO_{3-x} were unambiguously supported by the raman spectroscopy data. The raman spectra of the WO_3 nanosheets display three major characteristic peaks at 270, 715, and 805 cm^{-1}, arising from the bending vibration of $\delta_{(O–W–O)}$ and stretching vibrations of $\nu_{(W–O–W)}$ of the monoclinic phase, respectively [35]. However, the characteristic raman peaks for WO_{3-x} broaden after annealing, thus suggesting slight changes in its structure. After annealing, the W^{6+}–O stretching band at 270 and 715 cm^{-1} slightly shifted to lower wavelengths of 258 and 700 cm^{-1}. Similar results were reported in previous studies [35]. These results indicate that oxygen vacancies were successfully introduced to the nanosheets. The

formation of oxygen vacancies in the WO_3 crystals caused an up-shift of the W^{6+}-O bond in the raman spectrum, indicating that the structure of WO_{3-x} was changed by the formation of oxygen vacancies. These results are consistent with the HR-TEM images of WO_{3-x} (Figure 2d).

To further confirm the presence of oxygen vacancies in WO_{3-x}, electron paramagnetic resonance (EPR) spectroscopy was performed. EPR is highly sensitive to paramagnetic species containing unpaired electrons and it has been widely used to characterize oxygen vacancies. The test was performed at room temperature and the analytical results are shown in Figure 3d. It is evident that the WO_3 nanosheets did not contain any paramagnetic sites, as a flat line was observed in its EPR spectrum. In contrast, a strong EPR signal was observed at g = 2.01 and it could be ascribed to trapped electrons on oxygen vacancies in the WO_{3-x} [34,45].

The optical properties of the pristine WO_3 and WO_{3-x} nanosheets were examined by measuring their UV-Vis diffuse reflectance spectra, as shown in Figure 4. For the two samples, the steep increase in absorption at wavelengths shorter than ≈ 476 nm (2.6 eV) can be attributed to the intrinsic bandgap absorption of crystalline pristine WO_3. When examining the optical absorption beyond the band edge, WO_{3-x} possess a significant absorption in the visible and near infrared region. Notably, there is a broad absorption band from 400 to 1200 nm peaking at approximately 800 nm (see the inset of Figure 4). The absorption spectrum is similar to the reported results for $WO_{2.83}$ nanorods by Alivisatos et al. [46] and Meso-$WO_{2.83}$ by Thomas et al [45]. The enhanced visible light absorption peak in WO_{3-x} nanosheets samples can be undoubtedly assigned to the LSPR. The surface plasmon resonance in WO_{3-x} is correlated with its abundant free electrons. It is well known that even a very small decrease in oxygen content yields a dramatic increase in the electrical conductivity of WO_3. Consequently, oxygen vacancies provide abundant localized electrons in WO_{3-x} to support its plasmon resonance, in contrast to the pristine WO_3. Thus, we further estimated the free-carrier density from the LSPR peak, according to the Drude model [45,46].

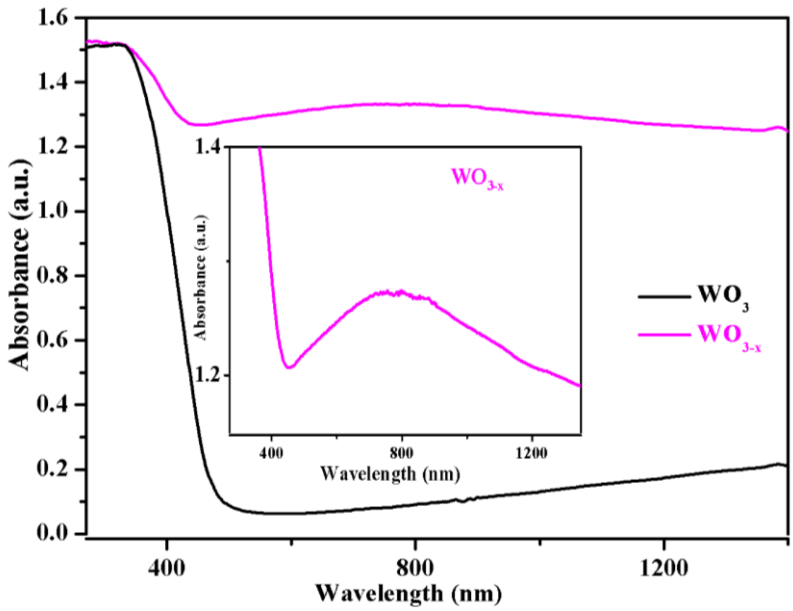

Figure 4. UV-Vis diffuse reflectance spectra of the WO_3 and WO_{3-x} nanosheets.

At the resonance condition, the plasmonic frequency, ω_{sp} can be expressed as:

$$\omega_{sp} = \sqrt{\frac{\omega_p{}^2}{1 + 2\varepsilon_m} - \gamma^2}, \quad (1)$$

where ω_p is the bulk plasma, ε_m is the dielectric constant of the surrounding medium, and γ is the damping parameter that is equal to the line width of the plasmon resonance band [45]. In our case, the value of ε_m is 1. For WO_{3-x}, the resonance energy is 1.55 eV at the plasmonic wavelength (800 nm) and the line width is 0.66 eV, as obtained by measuring the full width at half-maximum (FWHM) of the optical spectrum. Therefore, the bulk plasma frequency, ω_p, was estimated to be approximately 2.92 eV. Moreover, ω_p depends on the free electron density, N, by the formula:

$$\omega_P = \frac{Ne^2}{\varepsilon_0 m*} \tag{2}$$

where e is the elementary charge, ε_0 is the permittivity of free space, and m* is the effective mass of the free carriers. According to a previous report [46], the effective mass of WO_{3-x} is in the range of m_0 to 1.4 m_0. Therefore, the effective electron mass of WO_{3-x} was set to m* = 1.2 m_0, and m_0 represents the electron rest mass. Therefore, the free electron concentration, N, was estimated to be 9.1×10^{21} cm^{-3} in the WO_{3-x} sample. Table 1. summarizes the free electron concentration of a previously reported plasma-doped WO_{3-x}.

Table 1. The free electron concentration of a previously reported plasma-doped WO_{3-x}.

Plasmonic Materials	LSPR Wavelength	Free-Carrier Density (cm^{-3})	Reference
WO_{3-x}	800 nm	9.1×10^{21}	This Work
$WO_{2.83}$	650 nm	9.79×10^{21}	Ref. [45]
WO_{3-x}	1450 nm	2.5×10^{21}	Ref. [35]
WO_{3-x}	900 nm	6.3×10^{21}	Ref. [46]

X-ray photoelectron spectroscopy (XPS) was employed in order to investigate the transformation of surface chemical bonds and detect the electronic valence band position of the samples. The W $4f_{7/2}$ and $4f_{5/2}$ XPS peaks of WO_3 are centred at binding energies of 35.6 and 37.8 eV, respectively, as shown in Figure 5a, which is typical for W^{6+}–O bonds in WO_3 [35]. For WO_{3-x}, the W 4f XPS spectrum shows different features, where the W $4f_{7/2}$ and $4f_{5/2}$ peaks shift to higher energies at 35.9 and 38.1 eV, respectively (a shift of 0.3 eV). The XPS spectra of O 1s (Figure 5b) in the WO_3 samples show a well-developed peak at 530.4 eV, which can be attributed to the lattice oxygen. However, the O 1s XPS peak of WO_{3-x} (Figure 5b), which is located at ~530.7 eV, also showed a clear positive shift in binding energy of approximately 0.3 eV, which is consistent with shift that was observed in the W 4f peak. A reasonable explanation can be given for the shifting phenomena. Upon removal of an O atom, the nearest W atoms relax away from the vacancy, strengthening their bonding with the rest of the lattice. This outward relaxation decreases the overlap between the W dangling bonds and reduces the W–O bond length. To maintain the original crystal structure and stability, the W^{6+}–O bond binding energy was increased [47–49]. Reasonably, the positive shifts in the binding energies of W 4f and O 1s can be ascribed to the strong interaction between W^{6+} and oxygen vacancies. Van de Walle et al. showed that when the oxygen atoms are removed, the outward motion of the W atoms cause their bonds with the next-nearest-neighbour O atoms along the W–Vo–W direction to be compressed by up to 20%, through hybrid density functional theory [47]. Therefore, the positive shift of the XPS peak can be attributed to a shortening of the correlation length because of the presence of oxygen vacancies. Similar results have been reported for TiO_{2-x} by Dal Santo et al. [50]. They observed a lattice contraction of TiO_2 induced by the presence of oxygen vacancies.

The valence band (VB) position was analysed through the VB XPS spectra of the samples (Figure 5c). Both VB spectra were similar and the VB maxima were estimated by linear extrapolation of the peaks to the baselines, which derives a band edge position of 2.76 eV below the Fermi energy for both samples. The annealing treatment exerted a negligible effect on the VB position of the WO_{3-x} surface.

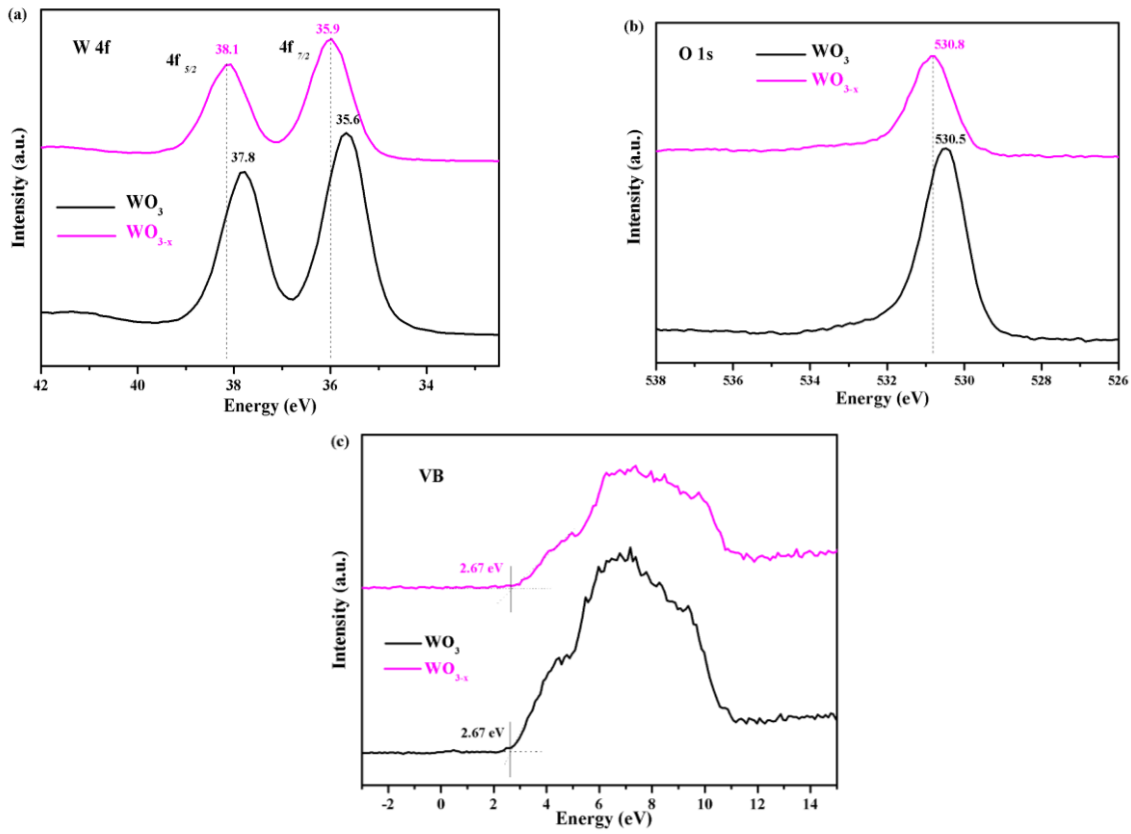

Figure 5. (**a**) The Ti 2p X-ray photoelectron spectra (XPS) spectra of the as-prepared WO_3 and WO_{3-x}; (**b**) O 1s XPS spectra of the as-prepared WO_3 and WO_{3-x} and (**c**) valence band (VB) XPS spectra of the as-prepared WO_3 and WO_{3-x}.

3.2. Photocatalytic Degradation Test

To evaluate the ability of the catalysts to degrade organic contaminants, RhB was used as a representative pollutant. The as-prepared WO_{3-x} photocatalysts are expected to exhibit considerable UV-light photocatalysis as compared to pristine WO_3. Before irradiation, an adsorption experiment was performed in the dark to ensure that adsorption equilibrium of RhB on the catalyst surface was adequately established. The results are shown in Figure 6a, where t, C, and C_0 refer to the irradiation time, instantaneous RhB concentration, and RhB concentration before irradiation, respectively. The C/C_0 ratio was used to describe the decomposition efficiency, which represents the concentration ratio before and after a certain period of reaction time. The WO_{3-x} sample efficiently decomposed the RhB in 80 min under in the irradiation of UV light, while the pristine WO_3 decomposed only approximately 30% of the RhB. The annealing-treated WO_{3-x} samples exhibited better photocatalytic activity than the pristine WO_3.

The photocatalytic activity of the WO_{3-x} sample was also investigated under visible light ($\lambda > 420$ nm) illumination. As shown in Figure 6b, the WO_3 samples showed little ability to decompose RhB after visible light irradiation for 320 min. In contrast, the WO_{3-x} samples exhibited higher photocatalytic efficiency (77%) than that of WO_3 (9%). The photocatalytic activity of visible light was greatly improved, because WO_{3-x} has enhanced visible light absorption at 400–1400 nm and the plasmonic effect due to the introduction of oxygen vacancies (Figure 3a). The oxygen vacancies were demonstrated to be electron donors and contributed to the enhanced donor density [44]. The increased donor density improved charge transport in WO_{3-x}. Therefore, the LSPR and charge transport are believed to be major mechanisms for the observed photocatalytic activity enhancement in the WO_{3-x} samples.

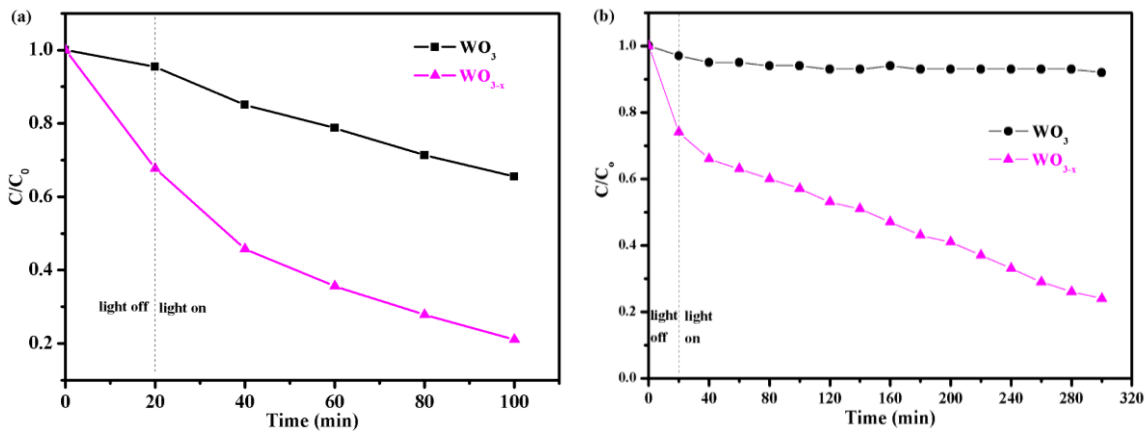

Figure 6. (**a**) UV light photocatalytic degradation of rhodamine B (RhB) and (**b**) visible-light photocatalytic degradation of RhB by the prepared photocatalysts.

4. Conclusions

We prepared monoclinic structured WO_3 nanosheets via a one-step template-free hydrothermal route and then introduced oxygen vacancies through low temperature annealing in alcohol. $_{-x}$ possesses a high concentration of oxygen vacancies, which were demonstrated to be electron donors and contributed to the enhanced donor density, which is believed to induce LSPR and to increase light harvesting efficiency in the visible and infrared regions. Simultaneously, the oxygen vacancies act as traps for reducing the recombination of electrons and holes and significantly improved the e-h separation efficiency, greatly enhancing the photocatalytic activity. This represents a novel approach for further improving the photocatalytic properties of WO_3. In addition, this study illustrates a facile route to obtain plasmonic WO_{3-x} nanosheets and may offer a generalized method for generating other semiconductor nanostructures with LSPR, such as deficient vanadium and molybdenum oxides.

Author Contributions: S.C. designed the study, analyzed the data, generated the figures and wrote the manuscript; Y.X. supervised rhodamine B products analysis in cooperation with S.C.; Y.W. conceived the concept, designed the experiments, analyzed the data and revised the manuscript; W.Z. revised the manuscript; Z.H. performed EPR analysis; H.Z. performed XPS analysis; W.X. performed FTIR and UV analysis.

Funding: This work is supported by the National Nature Science Foundation of China [No.21271048], Natural Science Foundation of China [11747074], Guangdong province science and technology plan project public welfare fund and ability construction project [2016A010103041, 2017A010103025], Doctoral Program of Lingnan Normal University [ZL1503], China Spark Program (2015GA780058).

Conflicts of Interest: The authors declare no conflict of interest.

References

1. Fujishima, A.; Honda, K. Electrochemical photolysis of water at a semiconductor electrode. *Nature* **1972**, *238*, 37–38. [CrossRef] [PubMed]
2. Chen, X.B.; Mao, S.S. Titanium Dioxide Nanomaterials: Synthesis, properties, modifications, and applications. *Chem. Rev.* **2007**, *107*, 289. [CrossRef] [PubMed]
3. Ma, Y.; Wang, X.; Jia, Y.; Chen, X.; Han, H.; Li, C. Titanium Dioxide-based nanomaterials for photocatalytic fuel generations. *Chem. Rev.* **2014**, *114*, 9987. [CrossRef] [PubMed]
4. Chen, X.; Shen, S.; Guo, L.; Mao, S.S. Semiconductor-based photocatalytic hydrogen generation. *Chem. Rev.* **2010**, *110*, 6503. [CrossRef] [PubMed]
5. Tada, H.; Kiyonaga, T.; Naya, S. Rational design and applications of highly efficient reaction systems photocatalyzed by noble metal nanoparticle-loaded titanium(IV) dioxide. *Chem. Soc. Rev.* **2009**, *38*, 1849. [CrossRef] [PubMed]
6. Dahl, M.; Liu, Y.; Yin, Y. Composite titanium dioxide nanomaterials. *Chem. Rev.* **2014**, *114*, 9853. [CrossRef] [PubMed]

7. Qu, Y.; Duan, X. Challenge and perspective of heterogeneous photocatalysts. *Chem. Soc. Rev.* **2013**, *42*, 2568. [CrossRef] [PubMed]
8. Asahi, R.; Morikawa, T.; Ohwaki, T.; Aoki, K.; Taga, Y. Visible-light photocatalysis in nitrogen-doped titanium oxides. *Science* **2001**, *293*, 269–271. [CrossRef] [PubMed]
9. Liu, G.; Zhao, Y.; Sun, C.; Li, F.; Lu, G.Q.; Cheng, H.M. Synergistic effects of B/N doping on the visible-light photocatalytic activity of mesoporous TiO_2. *Angew. Chem. Int. Ed.* **2008**, *47*, 4516–4520. [CrossRef] [PubMed]
10. Yang, G.D.; Jiang, Z.; Shi, H.H.; Xiao, T.C.; Yan, Z.F. Preparation of highly visible-light active N-doped TiO_2 photocatalyst. *J. Mater. Chem.* **2010**, *20*, 5301–5309. [CrossRef]
11. Hernández-Alonso, M.D.; Fresno, F.; Suáreza, S.; Coronado, J.M. Development of alternative photocatalysts to TiO_2: Challenges and opportunities. *Energy Environ. Sci.* **2009**, *2*, 1231. [CrossRef]
12. Fernández-Domene, R.M.; Sánchez-Tovar, R.; Lucas-Granados, B.; García-Antón, J. Improvement in photocatalytic activity of stable WO_3, nanoplatelet globular clusters arranged in a tree-like fashion: influence of rotation velocity during anodization. *Appl. Catal. B* **2016**, *189*, 266–282. [CrossRef]
13. Bai, X.; Sun, C.; Liu, D.; Luo, X.; Li, D.; Wang, J. Photocatalytic degradation of deoxynivalenol using graphene/ZnO hybrids in aqueous suspension. *Appl. Catal. B* **2017**, *204*, 11–20. [CrossRef]
14. Kudo, A.; Miseki, Y. Heterogeneous photocatalyst materials for water splitting. *Chem. Soc. Rev.* **2009**, *38*, 253. [CrossRef] [PubMed]
15. Zheng, H.; Ou, J.Z.; Strano, M.S.; Kaner, R.B.; Mitchell, A.; Kalantar-zadeh, K. Nanostructured tungsten oxide-properties synthesis, and applications. *Adv. Funct. Mater.* **2011**, *21*, 2175–2196. [CrossRef]
16. Chen, Q.; Li, J.; Zhou, B.; Long, M.; Chen, H.; Liu, Y.; Cai, W.; Shangguan, W.F. Preparation of well-aligned WO_3 nanoflake arrays vertically grown on tungsten substrate as photoanode for photoelectrochemical water splitting. *Electrochem. Commun.* **2012**, *20*, 153–156. [CrossRef]
17. An, X.; Yu, J.C.; Wang, Y.; Hu, Y.; Yu, X.; Zhang, G. WO_3 nanorods/graphene nanocomposites for high-efficiency visible-light-driven photocatalysis and NO_2 gas sensing. *J. Mater. Chem.* **2012**, *22*, 8525–8531. [CrossRef]
18. Ng, C.; Ng, Y.H.; Iwase, A.; Amal, R. Influence of annealing temperature of WO_3 in photoelectrochemical conversion and energy storage for water splitting. *ACS Appl. Mater. Interfaces* **2013**, *5*, 5269–5275. [CrossRef] [PubMed]
19. Reyes-Gil, K.R.; Wiggenhorn, C.; Brunschwig, B.S.; Lewis, N.S. Comparison between the quantum yields of compact and porous WO_3 photoanodes. *J. Phys. Chem. C* **2013**, *117*, 14947–14957. [CrossRef]
20. Hu, X.X.; Xu, P.Q.; Gong, H.Y.; Yin, G.T. Synthesis and characterization of WO_3/Graphene nanocomposites for enhanced photocatalytic activities by one-step in-situ hydrothermal reaction. *Materials* **2018**, *11*, 147.
21. Székely, I.; Kovács, G.; Baia, L.; Danciu, V.; Pap, Z. Synthesis of shape-tailored WO_3 micro-/nanocrystals and the photocatalytic activity of WO_3/TiO_2 composites. *Materials* **2016**, *9*, 258. [CrossRef] [PubMed]
22. Li, W.; Da, P.; Zhang, Y.; Wang, Y.; Lin, X.; Gong, X.; Zheng, G. WO_3 Nanoflakes for enhanced photoelectrochemical conversion. *ACS Nano* **2014**, *8*, 11770–11777. [CrossRef] [PubMed]
23. Osterloh, F.E. Cheminform abstract: Inorganic nanostructures for photoelectrochemical and photocatalytic water splitting. *Cheminform* **2013**, *42*, 2294–2320. [CrossRef]
24. Tanaka, A.; Hashimoto, K.; Kominami, H. Visible-light-induced hydrogen and oxygen formation over Pt/Au/WO_3 photocatalyst utilizing two types of photoabsorption due to surface plasmon resonance and band-gap excitation. *J. Am. Chem. Soc.* **2014**, *136*, 586–589. [CrossRef] [PubMed]
25. Xiang, Q.; Meng, G.F.; Zhao, H.B.; Zhang, Y.; Li, H.; Ma, W.J.; Xu, J.Q. Au nanoparticle modified WO_3 nanorods with their enhanced properties for photocatalysis and gas sensing. *J. Phys. Chem. C* **2010**, *114*, 2049–2055. [CrossRef]
26. Sun, S.M.; Wang, W.Z.; Zeng, S.Z.; Shang, M.; Zhang, L. Preparation of ordered mesoporous Ag/WO_3 and its highly efficient degradation of acetaldehyde under visible-light irradiation. *J. Hazard. Mater.* **2010**, *178*, 427–433. [CrossRef] [PubMed]
27. Cui, L.F.; Ding, X.; Wang, Y.G.; Shi, H.C.; Huang, L.H.; Zuo, Y.H.; Kang, S.F. Facile preparation of Z-scheme WO_3/g-C_3N_4 composite photocatalyst with enhanced photocatalytic performance under visible light. *Appl. Surf. Sci.* **2017**, *391*, 202–210. [CrossRef]
28. Jin, T.; Diao, P.; Wu, Q.Y.; Xu, D.; Hu, D.Y.; Xie, Y.H.; Zhang, M. WO_3 nanoneedles/α-Fe_2O_3/cobalt phosphate composite photoanode for efficient photoelectrochemical water splitting. *Appl. Catal. B* **2014**, *148–149*, 304–310. [CrossRef]

29. Momeni, M.M.; Ghayeb, Y.; Davarzadeh, M. Single-step electrochemical anodization for synthesis of hierarchical WO_3-TiO_2 nanotube arrays on titanium foil as a good photoanode for water splitting with visible light. *J. Electroanal. Chem.* **2015**, *739*, 149–155. [CrossRef]
30. Bazarjani, M.S.; Hojamberdiev, M.; Morita, K.; Zhu, G.Q.; Cherkashinin, G.; Fasel, C.; Herrmann, T.; Breitzke, H.; Gurlo, A.; Riedel, R. Visible light photocatalysis with c-WO_{3-x}/$WO_3 \cdot H_2O$ nanoheterostructures in situ formed in mesoporous polycarbosilane-siloxane polymer. *J. Am. Chem. Soc.* **2013**, *135*, 4467–4475. [CrossRef] [PubMed]
31. Song, J.J.; Huang, Z.F.; Pan, L.; Zou, J.J.; Zhang, X.W.; Wang, L. Oxygen-deficient tungsten oxide as versatile and efficient hydrogenation catalyst. *ACS Catal.* **2015**, *5*, 6594–6599. [CrossRef]
32. Yan, M.; Li, G.L.; Guo, C.S.; Guo, W.; Ding, D.D.; Zhang, S.H.; Liu, S.Q. WO_{3-x} sensitized TiO_2 spheres with full-spectrum-driven photocatalytic activities from UV to near infrared. *Nanoscale* **2016**, *8*, 17828–17835. [CrossRef] [PubMed]
33. Lou, Z.Z.; Xue, C. In situ growth of WO_{3-x} nanowires on g-C_3N_4 nanosheets: 1D/2D heterostructures with enhanced photocatalytic activity. *Cryst Eng Comm* **2016**, *18*, 8406. [CrossRef]
34. Li, Y.S.; Tang, Z.L.; Zhang, J.Y.; Zhang, Z.T. Defect engineering of air-treated WO_3 and its enhanced visible light-driven photocatalytic and electrochemical performance. *J. Phys. Chem. C* **2016**, *120*, 9750–9763. [CrossRef]
35. Yan, J.; Wang, T.; Wu, G.; Dai, W.; Guan, N.; Li, L.; Gong, J. Tungsten oxide single crystal nanosheets for enhanced multichannel solar light harvesting. *Adv. Mater.* **2015**, *27*, 1580. [CrossRef] [PubMed]
36. Lu, Y.; Jiang, Y.; Gao, X.; Wang, X.; Chen, W. Strongly coupled Pd nanotetrahedron/tungsten oxide nanosheet hybrids with enhanced catalytic activity and stability as oxygen reduction electrocatalysts. *J. Am. Chem. Soc.* **2014**, *136*, 11687. [CrossRef] [PubMed]
37. Wang, G.M.; Ling, Y.C.; Wang, H.Y.; Yang, X.Y.; Wang, C.C.; Zhang, J.Z.; Li, Y. Hydrogen-treated WO_3 nanoflakes show enhanced photostability. *Energy Environ. Sci.* **2012**, *5*, 6180. [CrossRef]
38. Chen, X.B.; Liu, L.; Yu, P.Y.; Mao, S.S. Increasing solar absorption for photocatalysis with black hydrogenated titanium dioxide nanocrystals. *Science* **2011**, *331*, 746–750. [CrossRef] [PubMed]
39. Cheng, H.F.; Wen, M.C.; Ma, X.C.; Kuwahara, Y.; Mori, K.; Dai, Y.; Huang, B.B.; Yamashita, H. Hydrogen doped metal oxide semiconductors with exceptional and tunable localized surface plasmon resonances. *J. Am. Chem. Soc.* **2016**, *138*, 9316. [CrossRef] [PubMed]
40. Hu, Y.H. A highly efficient photocatalyst-hydrogenated black TiO_2 for the photocatalytic splitting of water. *Angew. Chem. Int. Ed.* **2012**, *51*, 12410–12412. [CrossRef] [PubMed]
41. Zhang, H.L.; Yang, J.Q.; Li, D.; Guo, W.; Qin, Q.; Zhua, L.J.; Zheng, W.J. Template-free facile preparation of monoclinic WO_3 nanoplates and their high photocatalytic activities. *Appl. Surf. Sci.* **2014**, *305*, 274–280. [CrossRef]
42. Wu, H.Y.; Xu, M.; Da, P.M.; Li, W.J.; Jia, D.S.; Zheng, G.F. WO_3-reduced graphene oxide composites with enhanced charge transfer for photoelectrochemical conversion. *Phys. Chem. Chem. Phys.* **2013**, *15*, 16138. [CrossRef] [PubMed]
43. Li, Y.Y.; Wang, C.H.; Zheng, H.; Wan, F.X.; Yu, F.; Zhang, X.T.; Liu, Y.C. Surface oxygen vacancies on WO_3 contributed to enhanced photothermo-synergistic effect. *Appl. Surf. Sci.* **2017**, *391*, 654–661. [CrossRef]
44. Hilaire, S.; Süess, M.J.; Kränzlin, N.; Bieńkowski, K.; Solarska, R.; Augustyński, J.; Niederberger, M. Microwave-assisted nonaqueous synthesis of WO_3 nanoparticles for crystallographically oriented photoanodes for water splitting. *J. Mater. Chem. A* **2014**, *48*, 20530–20537. [CrossRef]
45. Cheng, H.F.; Klapproth, M.; Sagaltchik, A.; Li, S.; Thomas, A. Ordered mesoporous $WO_{2.83}$: Selective reduction synthesis, exceptional localized surface plasmon resonance and enhanced hydrogen evolution reaction activity. *J. Mater. Chem. A* **2018**, *6*, 2249. [CrossRef]
46. Manthiram, K.; Alivisatos, A.P. Tunable localized surface plasmon resonances in tungsten oxide nanocrystals. *J. Am. Chem. Soc.* **2012**, *134*, 3995–3998. [CrossRef] [PubMed]
47. Janotti, A.; Varley, J.B.; Rinke, P.; Umezawa, N.; Kresse, G.; Van de Walle, C.G. Hybrid functional studies of the oxygen vacancy in TiO_2. *Phys. Rev. B* **2010**, *81*, 085212. [CrossRef]
48. Morgan, B.J.; Watson, G.W. Intrinsic n-type defect formation in TiO_2: a comparison of rutile and anatase from GGA+U calculations. *J. Phys. Chem. C* **2010**, *114*, 2321. [CrossRef]

49. Pan, X.Y.; Yang, M.Q.; Fu, X.Z.; Zhang, N.; Xu, Y.J. Defective TiO_2 with oxygen vacancies: synthesis, properties and photocatalytic applications. *Nanoscale* **2013**, *5*, 3601–3614. [CrossRef] [PubMed]
50. Naldoni, A.; Allieta, M.; Santangelo, S.; Marelli, M.; Fabbri, F.; Cappelli, S.; Bianchi, C.L.; Psaro, R.; Dal Santo, V. Effect of nature and location of defects on bandgap narrowing in black TiO_2 nanoparticles. *J. Am. Chem. Soc.* **2012**, *134*, 7600. [CrossRef] [PubMed]